JOURNAL OF COMPUTATIONAL PHYSICS 46, 189–214 (1982)

Calculations of 3D Mirror Equilibria Using a Finite Element Vector Potential Representation*

D. V. ANDERSON, J. BREAZEAL, AND C. B. SHARP

National Magnetic Fusion Energy Computer Center,
Lawrence Livermore National Laboratory,
Livermore, California 94550

Received August 7, 1981; revised November 11, 1981

Several applications of plasma equilibrium models require a suitable continuous representation for the magnetic field. For example, numerical generation of single particle orbits in these fields requires that the continuum representation maintain $\nabla \cdot B = 0$ or at least keep it very small. Performing the interpolation analysis in terms of the vector potential **A** guarantees $\nabla \cdot \mathbf{B} = 0$, whereas using the magnetic induction **B** does not. The code presented here uses A as the primary dependent variable. A finite element representation employing tricubic splines significantly reduces spatial truncation errors compared to conventional finite difference methods. The theoretical equilibrium model allows pressure functions of the form $\mathbf{P}(B, \psi) = \hat{\mathbf{P}}(B)\,\omega(\psi)$. A modified long-thin approximation is derived which includes field line curvature effects; it agrees well with the results obtained from the code. Some results pertinent to the MFTF-B experiment are presented.

I. INTRODUCTION

We describe calculations of the VEPEC code which is documented in more detail in [1]. It is the third code in a hierarchy of computer programs which are used together to perform studies of particle confinement in high-beta mirror equilibrium fields. The other codes are ABCXYZ [2], TPSIC [3], and ORBXYZ [4]. These codes perform the following tasks:

(1) ABCBYZ: On a 3D Cartesian grid we generate the vector potential and magnetic induction field components from an arbitrary current-carrying coil arrangement. For example, we frequently use the yin–yang set in minimum-B devices such as 2XIIB or the MFTF plug. More complicated configurations such as TMX are also representable.

(2) TPSIC: A version of this code, SETORB, generates the tricubic spline coefficients for the fields generated by ABCXYZ. Two modes of operation are

* Work performed under the auspices of the U.S.D.O.E. by the Lawrence Livermore National Laboratory under contract W-7405-ENG-48.

0021-9991/82/050189-26$02.00/0

available in which we spline either the vector potential (**A**) or the magnetic induction (**B**).

(3) VEPEC: For the same $3D$ grid we take the spline representation of the vacuum vector potentials calculated in ABCXYZ and solve the plasma equilibrium problem given this vacuum field. Vector potentials from the plasma currents are calculated in the spline representation and added to the vacuum field values to represent the total equilibrium field vector potential. Magnetic induction is carried as a subsidiary derived field array.

(4) ORBXYZ: Given the tricubic spline representation of the fields it obtains $\mathbf{B} = \nabla \times \mathbf{A}$ (or $\mathbf{B} = \mathbf{B}$) at each orbit point at each time step depending on whether we splined **A**'s (or **B**'s). The particle is advanced using the GEAR solver [5] to evolve the Lorentz force. Detailed information regarding the magnetic moment, phase angles, etc., is generated and plots of the particle trajectory are made.

Calculations of $3D$ mirror plasma equilibria have been performed routinely for about ten years. The first codes developed about 1970 were based on simple plasma pressure models in which the dependence was $P_{||} = P_{||}(B)$ only [6, 7]. Recently, codes have been built extending these pressure models to $P_{||} = P_{||}(B, \psi)$, where ψ is a drift surface (or flux surface) label [8, 9].

One major application of these equilibrium codes is to provide self-consistent medium and high-beta magnetic fields to single-particle orbit codes which are used to study the confinement of the particles. Since mirror confinement is obtained by the approximate invariance of the magnetic moment μ, it is crucial to calculate μ accurately. From the definition of μ and Newton's equation the instantaneous evolution of μ is given by

$$\frac{1}{\mu}\frac{d\mu}{dt} = \frac{V_{||}}{B}\nabla \cdot \mathbf{B} - \frac{(V_\perp^2 + 2V_{||}^2)}{V_\perp}\frac{|\nabla_\perp \mathbf{B}|}{B}\cos\alpha \tag{1}$$

plus other terms [10]. Here α is the instantaneous-pase angle between $V_\perp$ and the $\mathbf{B} \times \nabla B$ direction. Physically (and in any continuum model), the first term vanishes; but in the numerical calculation of the particle orbit, $\nabla \cdot \mathbf{B} \neq 0$ can occur and then significant errors in μ are likely.

The particle pusher in the orbit code uses a very fine grid along the particle trajectory—the spacing is arbitrarily small compared to that of the field grid on which the fields are known. Errors due to this trajectory grid are likewise arbitrarily small compared to those produced by the field grid. When **B**'s are known on the field grid the interpolation formula chosen to get **B** at each orbit point will have $\nabla \cdot \mathbf{B} \neq 0$. For example, the conventional TIBRO code [11] produced this unwanted effect; it used *second order* Lagrange interpolation. Deriving interpolation formulae for **B** subject to the constraint $\nabla \cdot \mathbf{B} = 0$ leads to intractable nonlocal conditions on the spatial integrals of **B**; this suggests using the integrated variable **A**, the vector potential, for performing the analysis.

Using **A**'s we construct a $3D$ cubic-spline formula which has **A**, $\nabla\mathbf{A}$, and $\nabla\nabla\mathbf{A}$

continuous but third derivatives have discontinuities. Since $\nabla \cdot \mathbf{B} = \nabla \cdot (\nabla \times \mathbf{A}) = 0$ the formula also provides a continuous representation of $\nabla \cdot \mathbf{B} = 0$. The **B** at an orbit point is obtained by analytical differentiation of the cubic polynomial representation of **A**.

For the reasons outlined above we need a method to produce the **A**'s directly from a calculation of a self-consistent plasma equilibrium. Calculating **B**'s first will not work because inversion of the curl operation is not well defined; one cannot simply start with **B**'s and put $\mathbf{A} = (\nabla \times)^{-1}\mathbf{B}$, particularly in terms of discrete methods. Moreover, other equilibrium codes do not solve for **B**'s directly anyway. They solve for quasi-potentials difficult to relate to the vector potential numerically. So we must perform the equilibrium calculation in terms of **A**, keeping **B** only as a subsidiary derived quantity.

This report addresses the calculation of the **A**'s by the equilibrium code, VEPEC. The theoretical equilibrium model chosen is taken from Hall and McNamara [9] and allows pressure functions of the form $\mathbf{P} = \mathbf{P}(B, \psi) = \hat{\mathbf{P}}(B)\,\omega(\psi)$ consistent with the assumption of omnigenity. Our numerical algorithm, which solves for the vector potential, differs in several respects from the method employed in their code, MCGUS [9]. VEPEC, using a 3*D* finite element algorithm, has moderate memory requirements for obtaining good accuracy thus alleviating the requirement of disk memory.

In Section II we shall describe the equations which we solve by algorithms discussed in Section III. Section IV gives an analytic model for long-thin equilibria which include effects of finite curvature of the field lines. Section V gives results for a high beta stable equilibrium plasma of an MFTF-*B* plug, including a confirmation of omnigenity and an interesting property of the mirror mode threshold. Conclusions are presented in Section VI.

II. Model

As in many other equilibrium studies we assume charge neutrality, ignore the displacement current, and restrict ourselves to the time independent (equilibrium) case. Gaussian unit are used throughout.

One of Maxwell's equations (Ampere's law), in terms of the vector potential, is

$$\nabla^2 \mathbf{A}_{\mathrm{pl}} = \nabla^2 \mathbf{A}_{\mathrm{tot}} = -(4\pi/c)\mathbf{J}, \tag{2}$$

where $\mathbf{A}_{\mathrm{pl}}$ is the vector potential of the plasma currents alone and $\mathbf{A}_{\mathrm{tot}}$ is the total-vector potential. This equation assumes the Coulomb gauge $\nabla \cdot \mathbf{A}_{\mathrm{pl}} = \nabla \cdot \mathbf{A}_{\mathrm{tot}} = 0$.

The equation for pressure balance is

$$\nabla \cdot \mathbf{P} = (1/c)\mathbf{J} \times \boldsymbol{B}. \tag{3}$$

We use the notation of Hall and McNamara, where

$$\mathbf{b} = \mathbf{B}/B \tag{4}$$

is the unit vector along the field,

$$\mathbf{k} = -\mathbf{b} \cdot \nabla \mathbf{b} = \mathbf{b} \times (\nabla \times \mathbf{b}) \tag{5}$$

is the curvature vector, and

$$\eta = (4\pi/B^2)(P_\perp - P_{||}) = -(4\pi/B)(\partial P_{||}/\partial B) \tag{6}$$

is derived from the parallel component of Eq. (3) and is used to eliminate $P_\perp$ from the equations.

The pressure tensor is assumed to have the usual guiding-center fluid (GCF) two independent component form:

$$\mathbf{P} = P_\perp \mathbf{I} + (P_{||} - P_\perp)\mathbf{bb}. \tag{7}$$

If we substitute Eq. (7) into Eq. (3) and use Eqs. (4–6) we get:

$$(1/c)\mathbf{J} \times \mathbf{B} = \nabla \cdot \mathbf{P} = \nabla(P_{||} + \eta(B^2/4\pi)) - \mathbf{bB} \cdot \nabla(\eta B/4\pi) + \mathbf{k}(\eta B^2/4\pi). \tag{8}$$

To solve this equation for the current we cross Eq. (3) with $\mathbf{B}$ and find

$$\mathbf{B} \times (\nabla \cdot \mathbf{p}) = (1/c)\mathbf{B} \times (\mathbf{J} \times \mathbf{B}) = (\mathbf{J}B^2/c) - (1/c)\mathbf{B}(\mathbf{B} \cdot \mathbf{J}). \tag{9}$$

If we use Eq. (8) in Eq. (9) and solve for $\mathbf{J}$ we get

$$\mathbf{J} = \mathbf{bb} \cdot \mathbf{J} + \mathbf{B} \times [(c/B^2)\nabla(P_{||} + \eta(B^2/4\pi)) + \mathbf{k}\eta c/4\pi]. \tag{10}$$

Formally, this is

$$\mathbf{J} = \mathbf{J}_{||} + \mathbf{J}_\perp. \tag{11}$$

Then for the perpendicular part,

$$\mathbf{J}_\perp = \mathbf{B} \times [(c/B^2)\nabla(P_{||} + \eta(B^2/4\pi)) + \mathbf{k}\eta c/4\pi]. \tag{12}$$

Constraints on the Model

The physical requirement of no accumulation of charge demands $\nabla \cdot \mathbf{J} = 0$. We use this extra condition to compute a value for $J_{||}$ from

$$\nabla \cdot \mathbf{J} = \nabla \cdot \mathbf{J}_\perp + \nabla \cdot (J_{||}\mathbf{b}) = 0. \tag{13}$$

In the solution of Eq. (13), which is a first-order partial differential equation, only one boundary condition is required. Typically one would choose $J_{||} = 0$ at some surface $s = s_{\max}$ where there is no plasma. From the integral version of Eq. (13) one generally obtains $J_{||} \neq 0$ interior to the plasma as one integrates along a field line; and in general $J_{||} \neq 0$ at the plasma surface where that field line exits from the plasma volume. The admissible profiles are restricted to have $J_{||} = 0$ where the field line is exiting the plasma. In the theory of Hall and McNamara [9] omnigenity and

the physical constraints that $J_{||} = 0$ on the entire plasma surface is used to derive the following results:

Assume distribution functions of the omnigenous form:

$$\mathbf{f}(\mu, \varepsilon, J^*) = \omega(\alpha, \beta)\, \hat{F}(\mu, \varepsilon), \tag{14}$$

where μ, ε, and J^* are the usual adiabatic invariants with α and β the flux-line labels. So we obtain pressure profiles

$$P(\alpha, \beta, B) = \omega(\alpha, \beta)\, \hat{P}(B). \tag{15}$$

The constraint $\mathbf{J} = 0$ at the plasma surface is then shown to require a special form for the function ω, namely,

$$\omega(\alpha, \beta) = \omega(\bar{\Gamma}(\alpha, \beta)), \tag{16}$$

where

$$\nabla \cdot (\bar{\Gamma}\mathbf{B}) = 0. \tag{17}$$

The term $\bar{\Gamma}$ is often referred to, loosely, as the flux function or as the drift-surface label. Flux surfaces $\bar{\Gamma} = \bar{\Gamma}(\psi)$ are defined by $\bar{\Gamma}$.

At the midplane ($z = 0$), $\bar{\Gamma}$ is given by

$$\bar{\Gamma}(x, y, 0) = \hat{\Gamma}(x, y, 0) + \hat{\Gamma}(y, x, 0), \tag{18}$$

where $\hat{\Gamma}$ satisfies

$$\nabla \cdot (\hat{\Gamma}\mathbf{B}) = \hat{P}_{||} \tag{19}$$

throughout the volume of the domain. Details of these derivations are in [8].

The three equations of constraint. Eqs. (13), (17), and (19) are all of the form

$$\nabla \cdot (G\mathbf{B}) = S, \tag{20}$$

which is known as a magnetic-differential equation (MDE). Equation (19) provides the boundary condition for the solution of Eq. (17) which in turn provides the $\bar{\Gamma}$ surfaces upon which $\omega(\bar{\Gamma})$ depends. This allows Eq. (13) to be solved such that $J_{||}$ is zero everywhere on the plasma surface.

For completeness we write the defining relation for the magnetic induction **B**:

$$\mathbf{B} = \nabla \times \mathbf{A}_{\text{tot}}. \tag{21}$$

Equations (2), (12), (13), (17), (19), and (21) completely describe the equilibrium configuration in terms of **A**, **J**, and **B**.

Pressure Profiles

At present the code uses the pressure functions $\hat{P}_{||}(B)$ and $\hat{P}_{\perp}(B)$ from the Taylor model [12], where

$$\hat{P}_{||}(B) = CB(B_0 - B)^m, \qquad \hat{P}_{\perp}(B) = CB^2 m(B_0 - B)^{m-1} \tag{22}$$

or from the Rensink model [13], where

$$\hat{P}_{||}(B) = CB^{-m}(B_0 - B)^{m+3/2}, \qquad \hat{P}_{\perp}(B) = CB^{-m}(B_0 - B)^{m+1/2}[\tfrac{1}{2}B + (m+1)B_0] \tag{23}$$

or from the Cutler model [14] where

$$\hat{P}_{||}(B) = C(1 - (B/B_0) + (B/B_0)\ln(B/B_0)), \qquad \hat{P}_{\perp}(B) = C((B_0 - B)/B_0). \tag{24}$$

A choice of $m = 0.5$ or $m = 1$ is usually made for Eq. (23). The later two models (Eqs. (23) and (24)) have been shown to compare well with some Fokker–Planck results obtained from a bounce-averaged code [15]. In Figs. 1 and 2 we have shown these pressure profiles.

The function $\omega(\psi) = \omega(\bar{\Gamma})$ is read in as data along the x axis and can be arbitrarily set subject to the requirement that it be monotone decreasing in the radial (or x) coordinate and be nonnegative.

Inclusion of other pressure models is straightforward.

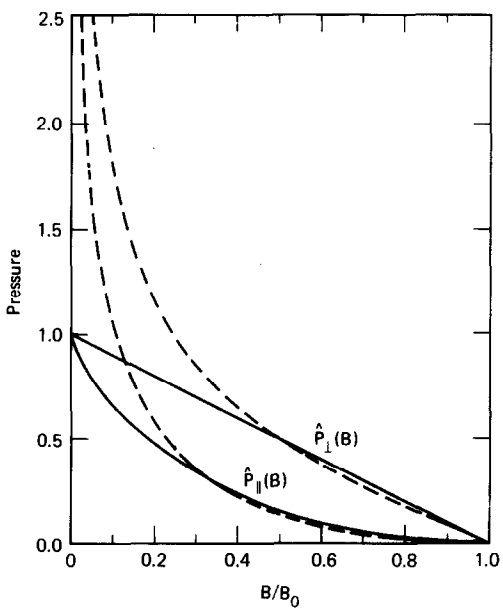

FIG. 1. The Rensink and Cutler pressure functions $\hat{P}_{\perp}(B)/C$ plotted versus B/B_0. (---, Rensink profile, $m = \frac{1}{2}$; —, Cutler profile.)

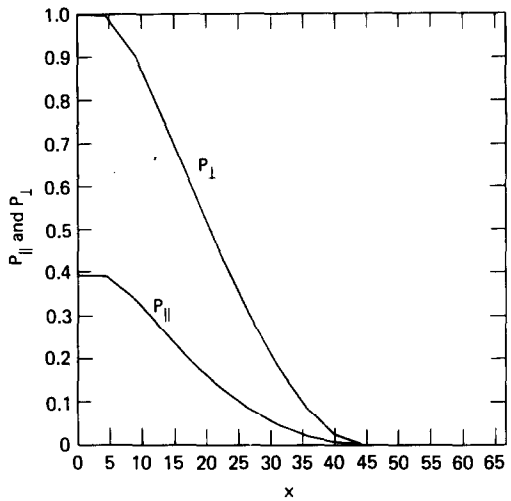

FIG. 2. The Rensink pressure profiles $\hat{P}_{\perp}(B)\,\omega(\bar{\Gamma})/C$ and $\hat{P}_{||}(B)\,\omega(\bar{\Gamma})/C$ are plotted versus x (a radial coordinate).

Coordinate Geometry and Boundary Conditions

Cartesian coordinates are used and octal symmetry is assumed. Specifically, by octal symmetry we mean

$$\frac{\partial A_x}{\partial x} = A_y = A_z = B_x = \frac{\partial B_y}{\partial x} = \frac{\partial B_z}{\partial x} = 0 \qquad \text{at} \quad x = 0, \tag{25a}$$

$$A_x = \frac{\partial A_y}{\partial y} = A_z = \frac{\partial B_x}{\partial y} = B_y = \frac{\partial B_z}{\partial y} = 0 \qquad \text{at} \quad y = 0, \tag{25b}$$

and

$$\begin{aligned} &A_x(x, y, -z) = -A_y(y, x, z), \qquad A_y(x, y, -z) = -A_x(y, x, z), \\ &A_z(x, y, -z) = A_z(y, x, z), \qquad B_x(x, y, -z) = -B_y(y, x, z), \\ &B_y(x, y, -z) = -B_x(y, x, z), \qquad B_z(x, y, -z) = B_z(y, x, z). \end{aligned} \tag{25c}$$

These conditions allow one to solve the equilibrium problem on the reduced domain defined by $x \geqslant 0$, $y \geqslant 0$, and $z \geqslant 0$ which is one octant of the field domain. Hence the name octal symmetry. These conditions give the boundary conditions to be used $x = 0$, $y = 0$, and $z = 0$. Fortunately, many minimum-B devices possess this octal symmetry; Baseball II, 2XIIB, MFTF, TMX, and reactor designs are prominent among these [16]. For example, Fig. 3 shows the MFTF yin–yang coil design which has this octal symmetry. Devices without octal symmetry could be treated by a straightforward modification of the code.

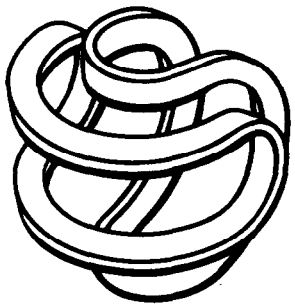

FIG. 3. A perspective view of the MFTF yin–yang coil set is shown. Each of the coils is a distorted baseball coil. Together these coils produce a minimum B field with octal symmetry.

Above we gave the boundary conditions at $x=0$, $y=0$, and $z=0$ which are satisfied by $\mathbf{A}_{\text{tot}}$, $\mathbf{A}_{\text{vac}}$, and $\mathbf{A}_{\text{pl}}$. At the outer boundaries—$x_{\max}$, $y_{\max}$, and $z_{\max}$—we must specify $\mathbf{A}_{\text{pl}}$ to make the boundary value problem complete. Physically, the plasma produced vector potential must be small at large distances—the so called far-field boundary condition. Since our boundaries are at best modest distances from the plasma we must approximate the plasma produced field there. To do this we obtain dipole and quadrupole moments of the plasma-current distribution which are then used in the multipole expansion to set the boundary values; i.e.,

$$\mathbf{A}_{\text{pl}}(\mathbf{x}) = \frac{\Pi \cdot \mathbf{x}}{r^3} + \frac{1}{2}\sum_{ij} Q_{ij}\frac{\mathbf{x}_i \mathbf{x}_j}{r^5}, \tag{26}$$

where

$$\begin{aligned} \Pi &= \int \mathbf{x}' J_{\text{pl}}(\mathbf{x}')\, d^3\mathbf{x}', \\ Q_{ij} &= \int (3\mathbf{x}'_i\, \mathbf{x}'_j - r^2\, \delta_{ij})\, J_{\text{pl}}(\mathbf{x}')\, d^3\mathbf{x}'. \end{aligned} \tag{27}$$

Here Π and Q are the dipole and quadrupole moment tensors, respectively.

III. COMPUTATIONAL METHOD

An iterative method is used to solve Eqs. (2), (12), (13), (17), (19), and (21). We distinguish two types of iteration: linear and nonlinear. The linear iterations refer to solution of Eq. (2) by holding the right side fixed. A nonlinear iteration refers to updated solutions of (12), (13), (17), (19), and (21) to allow us to calculate a new $\mathbf{J}$ for the right side of Eq. (2). Separate convergence criteria, in terms of residuals, are maintained for both types of iterations. When both have converged we have a

selfconsistent equilibrium solution. In the code, five primary subroutines are called to complete each full nonlinear iteration: BFIELD, PVAL, JVAL, MULTIPOLE, and AVECTSOLVE. Repeated calls to only AVECTSOLVE produce the linear iteration sequence.

Calculation of Magnetic Induction with BFIELD

BFIELD obtains $\mathbf{B} = \nabla \times \mathbf{A}$ by exact differentiation of the spline representation for $\mathbf{A} = \mathbf{A}_{vac} + \mathbf{A}_{pl}$. The spline coefficient arrays for the vacuum field $\mathbf{A}_{vac}$ are obtained from the codes ABCXYZ [2] (a relative of MAFCO [17]) and SETORB (TPSIC [3]). These respectively obtain the vector potential fields of the coils on the rectangular grid and subsequently transform these to spline representations. VEPEC solves directly for the spline coefficients of the plasma part of the field $\mathbf{A}_{pl}$ by solving difference equations derived in terms of these coefficients from the finite element model. The spline basis functions form the finite elements used here. The $3D$ cubic spline representation and the differentiation formula are given in the section describing the subroutine AVECTSOLVE.

Magnetic Differential Equation Solver

Before describing PVAL and JVAL we discuss the MDE (magnetic-differential equation) solver used in both of these routines. Equation (20) is the form to be solved. If we write it as an integral, then along a field line we get

$$G(\mathbf{x}) = \oint_{l(\mathbf{x}_0)}^{l(\mathbf{x})} \frac{S}{B}\, dl + G(\mathbf{x}_0). \tag{28}$$

The bilinear characteristic algorithm we use is based on this integral form. The field lines are the characteristics. To get G at a grid point $\mathbf{x}$ we simple follow the characteristic back to some known point $\mathbf{x}_0$. Since $\mathbf{x}_0$ is generally not a grid point we obtain $G(\mathbf{x}_0)$ from bilinear interpolation on a grid facet, where $\mathbf{x}_0$ is a point on that facet. To perform this, G must be previously defined at the corners of that facet. This can always be arranged if we start out with enough boundary data to make the MDE problems well posed. Once $G(\mathbf{x}_0)$ is determined then we set

$$G(\mathbf{x}) = \frac{S(\mathbf{x}) + S(\mathbf{x}_0)}{B(\mathbf{x}) + B(\mathbf{x}_0)} \Delta l + G(\mathbf{x}_0), \tag{29}$$

where

$$\Delta l = |\mathbf{x} - \mathbf{x}_0|.$$

For the simplest case of open field line confinement all of the characteristics have the same sign component along z; so the algorithm proceeds by scanning each subsequence $z =$ constant plane to determine $G(\mathbf{x})$ from the previous $z =$ constant plane by following the characteristics back to that plane to find $\mathbf{x}_0$. This method could be generalized for closed field lines but then the guiding center model is then not applicable.

Evaluation of Pressure and Current Profiles with PVAL *and* JVAL

PVAL generates $P_{||}(B, \bar{\Gamma})$ and $\eta(B, \bar{\Gamma})$ at each grid point. Once the grid dependence of $\bar{\Gamma}$ is known the formulae for P and η are trivially evaluated. Equations (17) and (19) are solved by the MDE solver to obtain $\hat{\Gamma}$ and $\bar{\Gamma}$, respectively.

JVAL is a long but straightforward subroutine evaluating **J** from Eqs. (12) and (13). The latter of these requires another MDE solution to obtain **J**. The MDE equivalent to Eq. (13) is

$$\nabla \cdot [(J_{||}/B)\mathbf{B}] = -\nabla \cdot \mathbf{J}_{\perp}. \tag{30}$$

Self-Consistent Boundary Conditions Obtained in Multipole

Subroutine MULTIPOLE evaluates Eq. (26) to determine the self-consistent fields at the outer boundaries. These boundary values are updated at every nonlinear iteration. Using these self-consistent boundary conditions changes the equilibrium solutions typically 5% compared to setting $\mathbf{A}_{\mathrm{pl}} = 0$ on the outer boundaries. Including octopole terms would have only a small effect (calculated in the code to be on the order of 0.01%)—so these are neglected.

These boundary conditions remove any doubt as to what confines the plasma. Using the simpler *perfectly conducting* boundary conditions implies that nonphysical image forces help confine the plasma. Such image forces neither persist in the experiments nor exist in the VEPEC modeling because of the self-consistent boundary conditions.

Solving the Nonlinear-Vector Poisson Equation in AVECTSOLVE

AVECTSOLVE solves Eq. (2) for Cartesian components of $\mathbf{A}_{\mathrm{pl}}$. It uses the Douglas–Gunn generalization [18] of the ADI [19] algorithm for the solution of parabolic partial differential equations [20]. In a future version we intend to use the ICCG [21] algorithm to speed up the calculation. To get Eq. (1) in parabolic form we add the term $\rho^*(\partial A/\partial t)$ so we are solving

$$\nabla^2 \mathbf{A}_{\mathrm{pl}} = -(4\pi/c)\mathbf{J} + \rho^* \, \partial \mathbf{A}_{\mathrm{pl}}/\partial t, \tag{31}$$

where ρ^* is a convergence parameter. AVECTSOLVE advances Eq. (31) one linear-iteration step (time step). Then we nonlinearly iterate by determining **B**, P, and **J** for the new **A**. Usually the nonlinear iteration is performed only after the linear iterations have partially converged. Towards the end of the calculation every iteration is nonlinear, i.e., **J** is updated every step. We iterate until the $\rho^* \, \partial A/\partial t$ term is negligible whence Eq. (31) becomes Eq. (2) and the $\mathbf{A}_{\mathrm{pl}}$ found is the solution of the equilibrium problem. The total-vector potential is obtained by adding on the vacuum part

$$\mathbf{A}_{\mathrm{tot}} = \mathbf{A}_{\mathrm{pl}} + \mathbf{A}_{\mathrm{vac}}. \tag{32}$$

Spline Formulae and the Algorithm for AVECTSOLVE

Lastly, we describe the finite element scheme used in AVECTSOLVE to solve Eq. (31). For any of the scalar components of Eq. (31) we write the equation in the form:

$$\nabla^2 F = g + \rho(F^{n+1} - F^n), \tag{33}$$

where

$$g = -(4\pi/c)\,J_x \quad \text{or} \quad -(4\pi/c)\,J_y \quad \text{or} \quad -(4\pi/c)\,J_z, \tag{34}$$

and

$$F = A_x \quad \text{or} \quad A_y \quad \text{or} \quad A_z. \tag{35}$$

The continuous finite element representation we employ for the vector potential fields is of the form

$$F(x, y, z) = \sum_l \sum_m \sum_n \alpha_{lmn} G_l(x)\, H_m(y)\, K_n(z). \tag{36}$$

Here G, H, and K are the basis functions appropriate to the finite element expansion. The piecewise continuous B-spline (cubic polynomial) basis functions are defined as

$$\begin{aligned}
G_l(x) &= 0, && x < x_{l-2},\\
&= (1/6\Delta x^3)(x - x_{l-2})^3, && x_{l-2} < x < x_{l-1},\\
&= (2/3) - (1/\Delta x^2)(x - x_l)^2 - (1/2\Delta x^3)(x - x_l)^3, && x_{l-1} < x < x_l,\\
&= (2/3) - (1/\Delta x^2)(x - x_l)^2 + (1/2\Delta x^3)(x - x_l)^3, && x_l < x < x_{l+1},\\
&= (1/6\Delta x^3)(x_{l+2} - x)^3, && x_{l+1} < x < x_{l+2},\\
&= 0, && x_{l+2} < x,
\end{aligned} \tag{37}$$

on a regular evenly spaced grid. H and K are defined similarly in terms of y and z.

Derivatives of these spline functions are calculated analytically to yield

$$\begin{aligned}
\frac{\partial G_l}{\partial x} &= 0, && x < x_{l-2},\\
&= (1/2\Delta x^3)(x - x_{l-2})^2, && x_{l-2} < x < x_{l-1},\\
&= -(2/\Delta x^2)(x - x_l) - (3/2\Delta x^3)(x - x_l)^2, && x_{l-1} < x < x_l,\\
&= -(2/\Delta x^2)(x - x_l) + (3/2\Delta x^3)(x - x_l)^2, && x_l < x < x_{l+1},\\
&= -(1/2\Delta x^3)(x - x_{l+2})^2, && x_{l+1} < x < x_{l+2},\\
&= 0, && x_{l+2} < x,
\end{aligned} \tag{38}$$

and

$$\begin{aligned}
\frac{\partial^2 G_l}{\partial x^2} &= 0, && x < x_{l-2}, \\
&= (1/\Delta x^3)(x - x_{l-2}), && x_{l-2} < x < x_{l-1}, \\
&= -(2/\Delta x^2) - (3/\Delta x^3)(x - x_l), && x_{l-1} < x < x_l, \\
&= -(2/\Delta x^2) + (3/\Delta x^3)(x - x_l), && x_l < x < x_{l+1}, \\
&= -(1/\Delta x^3)(x - x_{l+2}), && x_{l+1} < x < x_{l+1}, \\
&= 0, && x_{l+2} < x,
\end{aligned} \tag{39}$$

from exact differentiation of Eq. (37). At grid points we note the B-spline basis functions take on the special values:

$$\begin{aligned}
G_l(x_i) &= 0, && i < l-1, \\
&= \tfrac{1}{6}, && i = l-1, \\
&= \tfrac{2}{3}, && i = l, \\
&= \tfrac{1}{6}, && i = l+1, \\
&= 0, && i > l+1,
\end{aligned} \tag{40}$$

and the derivatives are

$$\begin{aligned}
\frac{\partial G_l}{\partial x}(x_i) &= 0, && i < l-1, \\
&= 1/2\Delta x, && i = l-1, \\
&= 0, && i = l, \\
&= -1/2\Delta x, && i = l+1, \\
&= 0, && i > l+1,
\end{aligned} \tag{41}$$

and

$$\begin{aligned}
\frac{\partial^2 G_l}{\partial x^2}(x_i) &= 0, && i < l-1, \\
&= 1/\Delta x^2, && i = l-1, \\
&= -2/\Delta x^2, && i = l, \\
&= 1/\Delta x^2, && i = l+1, \\
&= 0, && i > l+1.
\end{aligned} \tag{42}$$

These definitions generalize in a straightforward manner for a variably spaced grid.

The local nature of the basis functions means the individual sums in Eq. (36) cover only four terms at most. So at x_i, y_j, z_k we use Eq. (40) to get

$$F_{ijk} = F(x_i, y_j, z_k) = \sum_{l=i-1}^{i+1} \sum_{m=j+1}^{j+1} \sum_{n=k-1}^{k+1} (\alpha_{lmn}[\tfrac{2}{3} - \tfrac{1}{2}|l-i|][\tfrac{2}{3} - \tfrac{1}{2}|m-j|][\tfrac{2}{3} - \tfrac{1}{2}|n-k|]) \tag{43}$$

that has a total of 27 terms that can be regarded as involving the 27 nearest grid points which are the vertices of all the grid cubes containing the point i, j, k. Similarly, we can operate ∇^2 on F to get

$$\begin{aligned}(\nabla^2 F)_{ijk} &= \sum_{l=i-1}^{i+1} \sum_{m=j-1}^{j+1} \sum_{n=k-1}^{k+1} ((\alpha_{lmn}/\Delta x^2)[-2 + 3|l-i|][\tfrac{2}{3} - \tfrac{1}{2}|m-j|][\tfrac{2}{3} - \tfrac{1}{2}|n-k|] \\ &\quad + (\alpha_{lmn}/\Delta y^2)[\tfrac{2}{3} - \tfrac{1}{2}|l-i|][-2 + 3|m-j|][\tfrac{2}{3} - \tfrac{1}{2}|n-k|] \\ &\quad + (\alpha_{lmn}/\Delta z^2)[\tfrac{2}{3} - \tfrac{1}{2}|l-i|][\tfrac{2}{3} - \tfrac{1}{2}|m-j|][-2 + 3|n-k|]).\end{aligned} \tag{44}$$

Again this has 27 terms for the different α's.

From the foregoing it is clear that the basis functions are twice differentiability continuous with discontinuities in the third derivatives. This means both $\mathbf{B} = \nabla \times \mathbf{A}$ and $\nabla^2\mathbf{A}$ have continuous representations. Furthermore $\mathbf{J} = -(c/4\pi)\nabla^2\mathbf{A}$ is continuous and is in fact a trilinear spline. We must be careful to remember that $\mathbf{J} = \mathbf{J}(\mathbf{B})$ is a nonlinear function of $\mathbf{B}$ and will not give a linear representation between grid points. Of course it will be exact at the grid points. If one expands the nonlinear $\mathbf{J}$ in a Taylor series about any grid point, terms of order Δx^2 and higher are not representable by the trilinear splines. So the errors in the $\mathbf{J}$'s are second order in space. We write this as

$$\mathscr{E}(\mathbf{J}) = \mathbf{J}_{\text{spline}} - \mathbf{J}_{\text{exact}} \sim \Delta x^2 \qquad \text{etc.} \tag{45}$$

Since the $\mathbf{B}$ and $\mathbf{A}$ representations are exactly integrals of the $\mathbf{J}$ trilinear spline, the errors are correspondingly at higher orders:

$$\mathscr{E}(\mathbf{B}) \sim \Delta x^3 \qquad \text{etc.} \tag{46}$$

and

$$\mathscr{E}(\mathbf{A}) \sim \Delta x^4 \qquad \text{etc.} \tag{47}$$

This indicates that the accuracy for the vector potentials will be third order while the derived magnetic fields will be second order. In contrast, most conventional field solvers produce first order accuracy for the magnetic fields.

The method we use, the Douglas–Gunn algorithm, can only solve for the 7-point

operator. The contribution of the remaining 20 terms will be included explicitly in the iterations. Accordingly we break up the sums given in Eqs. (43) and (44) into two parts each:

$$F_{ijk} = F_{(7)ijk} + F_{(20)ijk} \tag{48}$$

and

$$(\nabla^2 F)_{ijk} = (\nabla^2 F)_{(7)ijk} + (\nabla^2 F)_{(20)ijk}. \tag{49}$$

With this notation, Eq. (33) becomes

$$(\nabla^2 F)_{(7)} = g + \rho(F^{n+1}_{(7)} - F^n_{(7)}) + \rho(F^{n+1}_{(20)} - F^n_{(20)}) - (\nabla^2 F^n)_{(20)}. \tag{50}$$

The subscripts i, j, k have been suppressed to avoid a cumbersome expression.

Since the converged steady solution of Eq. (50) has the ρ term vanishing we have freedom to change this term somewhat. So alternatively we may solve

$$(\nabla^2 F)_{(7)} = g + \rho(F^{n+1}_{(7)} - F^n_{(7)}) - (\nabla^2 F^n)_{(20)} \tag{51}$$

which shares the same converged solution as Eq. (50). It is convenient to define

$$g' = g - (\nabla^2 F^n)_{(20)}. \tag{52}$$

Then the system to solve is

$$(\nabla^2 F)_{(7)} = g' + \rho(F^{n+1}_{(7)} - F^n_{(7)}). \tag{53}$$

Now, these are really equations for the α's—the spline coefficients. It must be kept in mind that we do not store the F values at the grid points but that we store the spline coefficients (in keeping with the claim that we use a spline representation).

Let us define the discrete spatial operators ΔX, ΔY, and ΔZ by

$$\Delta X(\alpha_{ijk}) = (1/\Delta x^2)(\alpha_{i+1jk} - 2\alpha_{ijk} + \alpha_{i-1jk}), \tag{54}$$

and the others analogously in the y and z coordinates. From these we find

$$(\nabla^2 F)_{(7)} = (\Delta X + \Delta Y + \Delta Z)(\alpha_{ijk}). \tag{55}$$

Putting these together yields

$$(\Delta X + \Delta Y + \Delta Z)(\alpha_{ijk}) = g' + \rho(\alpha^{n+1}_{ijk} - \alpha^n_{ijk}), \tag{56}$$

where we have legitimately altered the ρ term yet again. This alteration is permissible because the ρ term preserves its sign and it vanishes anyway at convergence.

In Eq. (56) we have deliberately omitted the time levels on the left side to indicate that many choices for this assignment are acceptable. Our choice is given by the

Douglas–Gunn algorithm [18] which uses the following set of *half-implicit* difference equations:

$$\begin{aligned} &\tfrac{1}{2}\Delta X(\alpha^{n+1}+\alpha^n)+\Delta Y(\alpha^n)+\Delta Z(\alpha^n)=g'+\rho(\alpha^{n+1}+\alpha^n),\\ &\tfrac{1}{2}\Delta Y(\alpha^{n+1}-\alpha^n)=\rho(\alpha^{n+2}-\alpha^{n+1}),\qquad \tfrac{1}{2}\Delta Z(\alpha^{n+3}-\alpha^n)=\rho(\alpha^{n+3}-\alpha^{n+2}) \end{aligned} \tag{57}$$

and we again suppress the grid indices. This Douglas–Gunn method was chosen for its favorable numerical stability properties. Finally, we rearrange the equation with just the unknown quantities appearing on the left side:

$$\begin{aligned} &(\tfrac{1}{2}\Delta X-\rho)(\alpha^{n+1})=\tfrac{1}{2}\Delta X\alpha^n-\Delta Y\alpha^n+\Delta Z\alpha^n+g-\rho\alpha^n,\\ &(\tfrac{1}{2}\Delta Y-\rho)(\alpha^{n+2})=\tfrac{1}{2}\Delta Y\alpha^n-\rho\alpha^{n+1},\qquad (\tfrac{1}{2}\Delta Z-\rho)(\alpha^{n+3})=\tfrac{1}{2}\Delta Z\alpha^n-\rho\alpha^{n+2}. \end{aligned} \tag{58}$$

Each of the equations in (58) is a tridiagonal system of implicit difference equations in the indices i, j, and k, respectively. Each is solved by an ordinary tridiagonal solver. A separate subroutine TRIDIAG is employed by the code to perform this operation.

One restriction on the solution of Eq. (58) is that ρ (the convergence parameter) must be held constant as the α's are advanced from level n to level $n+3$.

IV. Finite Curvature Long-Thin Equilibrium Model

We define the plasma beta to be

$$\beta_\perp = 8\pi P_\perp(0,0,0)/B^2_{\text{vac}}(0,0,0). \tag{59}$$

The equilibrium equation (3) can be put in the form

$$\nabla_\perp(P_\perp+(B^2/8\pi))=\mathbf{k}((B^2/4\pi)+P_\perp-P_{||}). \tag{60}$$

Sometimes the curvature $\mathbf{k}$ can be neglected because the plasma is confined to field lines near the axis which are nearly straight. This assumption leads to the well-known long-thin equilibrium, where

$$P_\perp(x,y,z)+(B^2/8\pi)(x,y,z)=(B^2_{\text{vac}}/8\pi)(0,0,z)). \tag{61}$$

If this is evaluated at $x=y=z=0$, then with Eq. (59) we can get the mirror ratio enhancement,

$$R_c/R_v = B_{\text{vac}}(0,0,0)/B_{\text{eq}}(0,0,0)=(1-\beta_\perp)^{-1/2}. \tag{62}$$

To get a better approximation we must include the effect of field line curvature. We start with Eq. (60) writen along the midplane diagonal where the quadrupole

symmetries force the $\nabla_\perp$ direction to be purely radial. So for minimum-B fields, $\mathbf{k} = -\hat{r}|\mathbf{k}|$. With this, Eq. (60) may be written

$$\frac{\partial}{\partial r}(P_\perp + (B^2/8\pi)) = k((B^2/4\pi) + 2P_\perp - (P_\perp + P_{||})). \tag{63}$$

To make headway we assume the curvature k to be linear in r. So for the vacuum field:

$$k = c_v r, \tag{64}$$

where $c_v = \partial k/\partial r$ at $r = 0$. For the effect of finite-plasma beta we adjust k with a factor $\theta = \theta(\beta_\perp)$ and write

$$k = c_v \theta r. \tag{65}$$

Of course $\theta = 1.0$ for a vacuum field. For higher beta plasmas where the field lines are straighter $\theta < 1.0$ is correct. We approximate the dependence on $\beta_\perp$ with

$$\theta = 1 - (1 - \alpha)\beta_\perp. \tag{66}$$

At $\beta_\perp = 1.0$, we see $\theta = \alpha$. We call α the coefficient of curvature decrement at $\beta_\perp = 1.0$. Experience from the numerical solutions for the equilibria or other insights might give good estimates for α. We make the crude assumption that $\beta_\perp = 1.0$ will just straighten the field lines at the midplane making both k and θ zero. So we put

$$\alpha = 0. \tag{67}$$

To solve Eq. (63) we make the substitutions:

$$W = P_\perp + (B^2/8\pi), \tag{68}$$

$$U = (B^2/8\pi)_{\text{vac}}, \tag{69}$$

and

$$D = \tfrac{1}{2}(P_\perp + P_{||}). \tag{70}$$

With these substitutions Eq. (63) becomes

$$\partial W/\partial r = 2c_v \theta r(W - D). \tag{71}$$

Let $s = r^2$, so we have

$$\partial W/\partial s = c_v \theta(W - D). \tag{72}$$

We make the further assumption that D is a linear decreasing function in s going to zero at the plasma surface $s_p = r_p^2$.

$$D = D_0(1 - (s/s_p)). \tag{73}$$

The resulting equation,

$$(\partial W/\partial s) - c_v \theta W = -c_v \theta D_0 + c_v \theta D_0 (s/s_p), \tag{74}$$

can be solved as it is a simple first order inhomogeneous-ordinary differential equation. Its solution is

$$W = W_0' \exp(c_v \theta s) + (D_0/c_v \theta s_p)[c_v \theta (s_p - s) - 1]. \tag{75}$$

For the vacuum field in the absence of plasma we have the special case:

$$U = U_0' \exp(c_v s). \tag{76}$$

At the plasma surface, $s = s_p$ the equilibrium and the vacuum field are very nearly the same so

$$U = W - \varepsilon, \tag{77}$$

where ε is the small discrepancy. On the axis at $s = 0$,

$$U_0 = U_0' \qquad \text{and} \qquad W_0 = W_0' + D_0[1 - (1/c_v \theta s_p)]. \tag{78}$$

Combining Eqs. (75) through (78) we get

$$\varepsilon + U_0 \exp(c_v s_p) = [W_0 - D_0(1 - (1/c_v \theta s_p))] \exp(c_v \theta s_p) - (D_0/c_v \theta s_p). \tag{79}$$

For reasonable values of $c_v s_p = k_{vac} r < 1.0$ we can expand the exponentials to obtain an equation first order in $c_v s_p$:

$$\varepsilon + U_0(1 + c_v s_p) = W_0(1 + c_v \theta s_p) - D_0(\tfrac{1}{2} c_v \theta s_p). \tag{80}$$

In first order we can also use

$$1/(1 + c_v \theta s_p) = 1 - c_v \theta s_p. \tag{81}$$

It is also convenient to define the betas:

$$\beta_\perp = 8\pi P_\perp / B_{vac}^2(0), \qquad \beta_{||} = 8\pi P_{||}/B_{vac}^2(0), \qquad \beta_\varepsilon = 8\pi\varepsilon/B_{vac}^2(0). \tag{82}$$

Now divide Eq. (80) by $B_{vac}^2(0)/8\pi$ and use Eqs. (81) and (82) together with the definitions given by Eqs. (68)–(70). Then,

$$\beta_{||} + (\beta_{eq}^2(0)/B_{vac}^2(0)) = [\rho_\varepsilon + (1 + c_v s_p) + \tfrac{1}{4}(\beta_\perp + \beta_{||})\, c_v \theta s_p](1 - c_v \theta s_p). \tag{83}$$

The mirror ratio enhancement is just

$$R_e/R_v = B_{vac}(0)/B_{eq}(0) \tag{84}$$

if we assume the self-fields at the mirror position are small. If we solve Eq. (83) for R_e/R_v keeping terms only to first order we get,

$$R_e/R_v = [1 - \beta_\perp + \beta_\varepsilon(1 - c_v \theta s_p) + c_v s_p(1 - \theta + \tfrac{1}{4}(\beta_\perp + \beta_{||})\theta)]^{-1/2} \tag{85a}$$

$$R_e/R_v = [1 - \beta_\perp + \beta_\varepsilon(1 - c_v(1 - \beta_\perp)\, s_p) + c_v c_p(\beta_\perp + \tfrac{1}{4}(\beta_\perp + \beta_{||})(1 - \beta_\perp))]^{-1/2} \tag{85b}$$

$$R_e/R_v = [1 - \beta_\perp + \beta_\varepsilon(1 - c_v s_p) + \tfrac{1}{4} c_v s_p(\beta_\perp + \beta_{||})]^{-1/2}, \tag{85c}$$

where the latter forms use Eq. (66) with $\alpha = 0$ and $\alpha = 1$, respectively.

The long-thin version (with no curvature) is obtained by letting c_v and β_ε go to zero. Only the later condition is nearly always a good assumption as we have found $\beta_\varepsilon < 0.04$ in most circumstances. In these limits we recover the conventional long-thin formula:

$$R_e/R_v = [1 - \beta_\perp]^{-1/2} \tag{86}$$

which is just Eq. (62).

In Fig. 4 we show plots of Eqs. (85b), (85c), and (86). On this plot we also mark the results obtained from equilibrium solutions calculated by VEPEC; the letter "x"

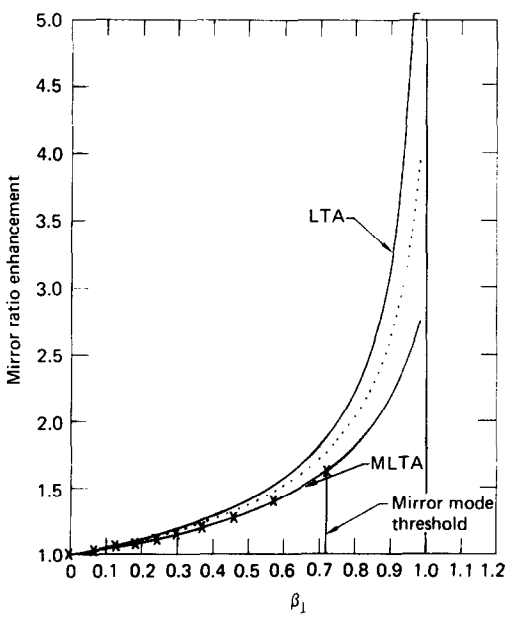

FIG. 4. The long-thin (LTA) and modified long-thin (MLTA) formulae for the MFTF configuration are plotted showing the mirror ratio enhancement as a function of $\beta_\perp$. The lowest curve is a plot of Eq. (86b). The top curve is the long-thin formula and the middle curve plots Eq. (86c). The x symbol shows several equilibria computed by VEPEC for various betas up to the mirror mode threshold. Agreement with the modified long-thin formula, Eq. (86b), is excellent beause the field line curvature is small enough to make the approximation we use very good.

indicates the results calculated for a MFTF plug configuration at various betas below the mirror mode threshold. It fits the modified long-thin formula Eq. (85b) very well indicating the choice of equilibrium curvature decrement in Eq. (67) is reasonable. We see that the ordinary long-thin formula is poor by comparison.

V. Results from VEPEC for Yin–Yang Configurations

Several mirror devices have been modeled with VEPEC including Baseball II, 2XIIB, MFTF, and various fusion-reactor designs. The results shown here will be for the MFTF yin–yang coil and for pressure models consistent with the neutral beam-generated plasma's distribution function. We have tested the resultant equilibria and found that the assumption of omnigenity is consistent. These tests were performed with ORBXYZ [4] which followed single particles and showed drift surfaces of the omnigenous form.

In Fig. 5 we display the depressed equilibrium mod-B contours in the MFTF well for a case just below the mirror mode threshold and compare them with the vacuum field. Figure 6 shows the axial and radial profiles of B_{vac} and B_{eq}. We have also obtained results which show a straightening of the flux lines near the midplane and near the axis. This effect was used in Eq. (66).

Equilibria Near the Mirror-Mode Threshold

A limitation on the maximum $\beta_\perp$ is the mirror mode threshold for the onset of a loss of equilibrium. This is given as,

$$\begin{aligned} B + 4\pi(\partial P_\perp/\partial B) < 0, &\qquad \text{no equilibrium,} \\ > 0, &\qquad \text{stable equilibrium.} \end{aligned} \tag{87}$$

It is convenient to use the *total perpendicular stress*

$$\Pi = P_\perp + B^2/8\pi. \tag{88}$$

As a function of B, Π has positive (negative) slope where the mirror mode conditions gives stable equilibrium (loss of equilibrium). Figure 7 shows a pressure model for several C values plotted in terms of Π versus $B^2/8\pi$. The curves labeled L and H give possible equilibria according to the long-thin model and the modified long-thin model as given in Eqs. (85b) and (86), respectively. Regions of possible equilibria are given by the intersection of these curves with the Π curves. A different graph of this sort exists for each choice of coil configuration and pressure model; the one shown here is for the MFTF device. The plot shows the long-thin approximation has a limit $\beta_\perp = 0.70$ for the mirror mode but the higher order approximation has its mirror mode limit at $\beta_\perp = 0.73$. An actual calculation of this equilibria at its mirror threshold was given by the rightmost x in Fig. 4 in good agreement with the higher order approximation.

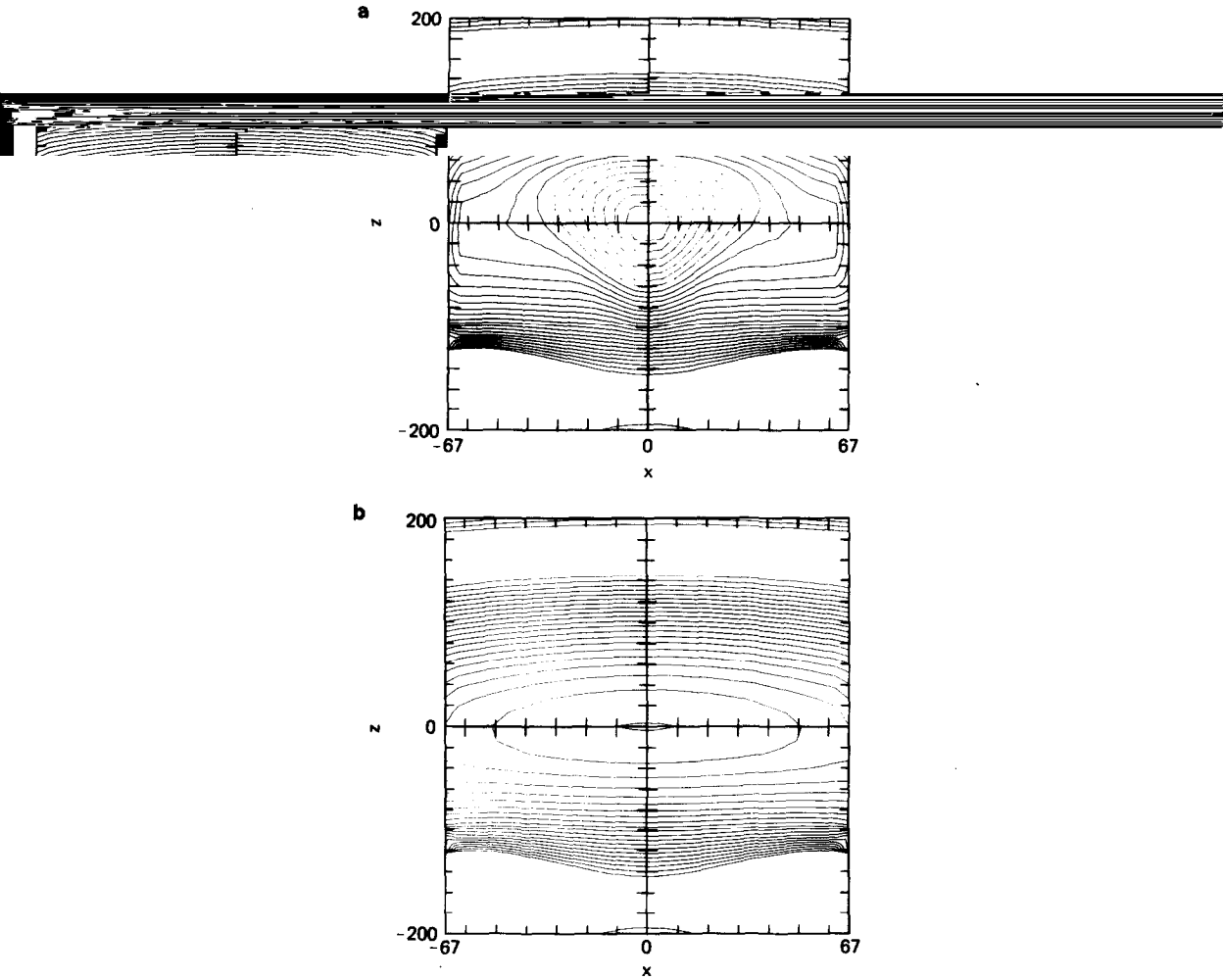

FIG. 5. We show the MFTF mod B contours in the x, z plane near the mirror mode threshold in (a) and for the vacuum case in (b).

One of the code diagnostics is a test on the mirror mode and firehose mode thresholds. In practice we do not encounter the firehose threshold for most pressure profiles but the mirror mode is nearly always encountered for sufficiently high $\beta_\perp$. The value of C in Eq. (22) which produces an equilibrium at the mirror mode threshold is denoted CDMM in the code. In one mode of operation C is adjusted during the iterations until it gives an equilibrium at, or just below the mirror mode threshold, where $C = \text{CDMM}$. Alternatively, lower beta equilibria are found by running the code with C fixed as some fraction of the mirror mode value $C = CS*\text{CDMM}$. CS gives that fraction. Typically, when given a vacuum field and a

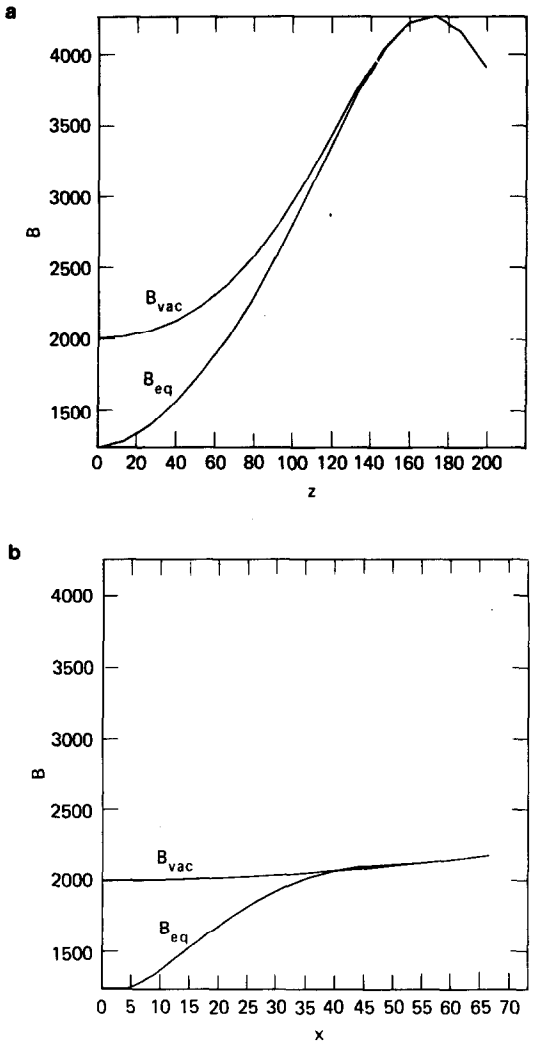

FIG. 6. Both vacuum and equilibrium B profiles are plotted against (a) the axial coordinate z and (b) the radial coordinate x.

pressure model, we calculate the mirror mode equilibrium first using the version of the code which automatically adjusts C until $C = \text{CDMM}$. Then for subsequent runs we use the CDMM calculated here and specify some $CS < 1$ to get equilibria below the mirror mode threshold.

It is well known that the mirror mode condition is the threshold for lack of existence of the solution rather than being an instability criterion [7]. We find, in agreement with this, that the code fails to converge for cases where $CS > 1 + \varepsilon$, where ε is an error of a percent or so. Below the mirror mode we have always been

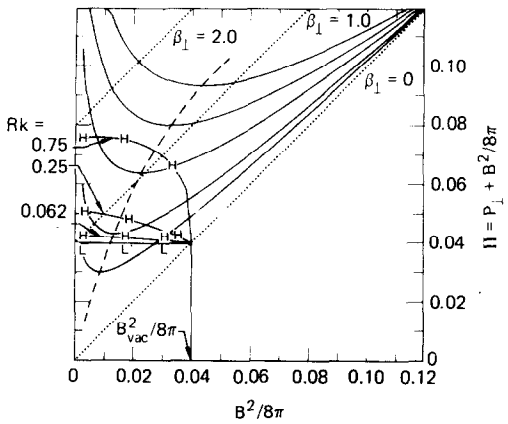

FIG. 7. Total perpendicular stress, $P_\perp + B^2/8\pi$ is plotted versus magnetic pressure, $B^2/8\pi$, for the Rensink profile $m = 1/2$. Several solid curves (—) are shown each for a different value C. Dotted lines (···) give iso-beta contours. Lines labeled "L" and "H" indicate results of the approximate equilibrium models obtained from the long-thin approximation (LTA) and from the modified long-thin approximation (MLTA), respectively. The different H curves are marametrized by Rk, the product of the vacuum curvature and plasma midplane radius at the plasma surface; $Rk = .062$ pertains to MFTF for the assumed ω profile. The minimum of each solid curve is the mirror mode threshold (---); a line connecting these minima is also shown. Its intersection with the "L" or "H" curves indicate what maximum $\beta_\perp$ is obtainable for each plasma configuration.

able to obtain converged equilibria for suitable values of the convergence parameter ρ.

The code shows an interesting property at the mirror-mode threshold for the Rensink pressure profile whenever $\omega(\psi)$ is flat near $r = 0$ (it has always been flat enough). We have detected the field-line curvature changing sign at this point, tending towards bad curvature as the threshold is exceeded.

This can be shown analytically as well. The demonstration starts with Eqs. (15) and (60) which can be combined to get

$$\nabla_\perp \Pi = \nabla_\perp \psi \, \partial \Pi/\partial \psi = \nabla_\perp \psi [\hat{P}_\perp(B) \, \partial \omega/\partial \psi] + \nabla_\perp B \, \partial \Pi/\partial B = \mathbf{k}_\psi ((B^2/4\pi) + P_\perp - P_{||}). \tag{89}$$

For most pressure profiles near the axis,

$$\partial \omega/\partial \psi = 0,$$

so

$$\nabla_\perp \Pi = \nabla_\perp B[(\partial P_\perp/\partial B) + (B/4\pi)], \tag{90}$$

or

$$\nabla_\perp B[(\partial P_\perp/\partial B) + (B/4\pi)] = k_\psi ((B^2/4\pi) + P_\perp - P_{||}). \tag{91}$$

The factor in brackets is just the mirror mode criteria. Since the expression in parenthesis in Eq. (91) is positive definite for the Rensink profiles, then we see that $[\,] = 0$, implies $k_\psi = 0$. This indicates the straightening of a field line near the axis—just the effect seen in the code results.

Applications of VEPEC *Results in Fokker–Planck Calculations*

When finite-beta effects are included in Fokker–Planck studies the relationship of $\beta_\perp$ to R_e/R_v is required. Knowledge of the maximum $\beta_\perp$ and its relationship to the enhancement of the longitudinal mirror ratio R_e/R_v can be obtained from the code if it can not be obtained from the formulae, Eqs. (84) and (85), derived above. It is expected that the equilibrium results can be used to generate an empirical formula for this relationship which will allow more realistic collisional studies to be performed by the Fokker–Planck codes.

A's Versus B's in Orbit Studies

Confinement studies require the detailed structure of the equilibrium fields. The analytic theory of adiabaticity uses fits to the equilibrium field to determine energy limits for adiabatic confinement. In fact, the specific application for which VEPEC has been developed is to provide the single particle orbit code ORBXYZ [4] with the equilibrium vector potential fields for performance of confinement studies. We re-emphasize the fact that $\nabla \cdot \mathbf{B} \neq 0$ effects interfere with these studies and use of vector potentials allows one to get $\nabla \cdot \mathbf{B} = 0$ accurate to computer roundoff. An example of this difficulty follows.

A comparison between orbits run by ORBXYZ with vector potentials versus magnetic induction has been made using the equilibrium **A**'s and **B**'s generated by VEPEC for the MFTF configuration [4]. At $\beta_\perp = 0.64$ the fields produced were used to study the trajectory of a fusion energy, $\varepsilon = 50$ keV, deuteron. After following each orbit for a drift period an estimate of the nonadiabatic effects is made and a confinement time calculated. The particle confined by the **A**'s lived about 1000 times longer than the particle run using the **B**'s; this shorter lifetime is shown to be due to $\nabla \cdot \mathbf{B} \neq 0$. Detailed printout of the interpolated values for B at the orbit points show $\nabla \cdot \mathbf{B}$ contributes more to $\Delta\mu$ than the other physical sources of nonadiabaticity when **B**'s are used on the grid. When **A**'s are used the printout shows $\nabla \cdot \mathbf{B} = 0$ accurate to computer roundoff, that is $\nabla \cdot \mathbf{B}$ is down 13 order of magnitude compared to the other gradients of **B**.

VI. Conclusions

VEPEC is now a useful, inexpensive tool in the calculation of mirror equilibrium plasma configurations. It and the code MCGUS are providing input to other theoretical models of the mirror configurations. In providing realistic equilibrium plasma profiles it can be used to help:

(1) Study micro-instabilities as it provides the background state.

(2) Study MHD interchange and ballooning instabilities.

(3) Give Fokker–Planck models $R_e = R_e(\beta_\perp)$ either directly from the code or indirectly from the modified long-thin formula (MLTA) as confirmed by VEPEC calculations.

(4) Study adiabatic confinement analytically.

(5) Study confinement with orbit codes.

(6) Estimate neutron fluxes at first walls.

In turn these studies might be used to optimize reactor designs.

Several limitations of the VEPEC model should be noted. We divide them into groups according to whether the problem is fundamental or can be remedied in future versions of the code and/or computers. Among the fundamental limitations are:

(1) The model is restricted to guiding center, two pressure component, small gyro-radius plasmas. This means we are unable to study field-reversed plasmas.

(2) The model is restricted to pressure functions of the product form consistent with omnigenity.

(3) Steady-flow equilibria are not permitted.

Some remediable restrictions are:

(1) No model for ambipolar potential is included.

(2) We are limited to the Douglas–Gunn algorithm. One could incorporate the ICCG [21] algorithm into VEPEC; it should be about an order of magnitude faster based on tests we performed with a $3D$ nonlinear Poisson solver using ICCG. Its convergence properties were superior to the Douglas–Gunn algorithm in this test; we would expect this improvement to carry over to the VEPEC calculations.

(3) Octal symmetry is assumed. Larger computer memories would allow treatment of the general $3D$ nonsymmetric case. For example, Stellerators might be a candidate for study.

One of the most favorable features of the code is its speed and ability to converge quickly to solutions far away from the initial iterates. It does not have any disk or tape manipulation required during execution which accounts in part for its speed advantage over MCGUS. Being core bound in the CDC 7600, however, it is limited to a coarser mesh with $21 \times 21 \times 21$ being nearly the limit—MCGUS has a somewhat finer mesh with $32 \times 32 \times 32$ as its upper limit. If we take $h = \Delta x/x_{\max} = \Delta y/y_{\max} = \Delta z/z_{\max}$, then in the long wavelength limit the MCGUS truncation error for $\mathbf{B}$ is proportional to $h^2 = 1/900$. VEPEC, with its higher order errors has $h^3 = 1/8000$ for comparison. For shorter wave lengths the improvement is less. The errors are comparable at wavelengths of the order of two grid cells. Since most pressure functions have mostly long wavelength structure we expect VEPEC to be sufficiently accurate. A CRAY-1 version is being developed.

ACKNOWLEDGMENTS

The authors thank J. K. Boyd, L. S. Hall, and B. McNamara for useful discussions. We are particularly indebted to M. E. Rensink for many valuable suggestions. This work would not have been completed without the resources and encouragement of the Physics group of the National Magnetic Fusion Energy Computer Center.

This document was prepared as an account of work sponsored by an agency of the United States Government. Neither the United States Government nor the University of California nor any of their employees, makes any warrantly, express or implied, or assumes any legal liability or responsibility for the accuracy, completeness, or usefulness of any information, apparatus, product, or process disclosed, or represents that its use would not infringe privately owned rights. Reference herein to any specific commercial products, process, or service by trade name trademark, manufacturer, or otherwise, does not necessarily constitute or imply its endorsement, recommendation, or favoring by the United States Government or the University of California. The views and opinions of authors expressed herein do not necessarily state or reflect those of the United States Government thereof, and shall not be used for advertising or product endorsement purposes.

REFERENCES

1. D. V. ANDERSON, J. BREAZEAL, AND C. B. SHARP, "*VEPEC: A 3D Vector Potential Equilibrium Code for High-beta Minimum-B Plasma Confinement*," Lawrence Livermore National Laboratory Report UCRL-53099, 1981.
2. D. V. ANDERSON, J. BREAZEAL, C. H. FINAN, AND B. M. JOHNSON, "*The* ABCXYZ *Code for Computing Vector Potential and Magnetic Fields from General Current Elements*," Lawrence Livermore Laboratory Report UCRL-52029, 1976.
3. D. V. ANDERSON, "*The Three-Dimensional Tensor Product Spline Interpolation Code* (TPSIC)," Lawrence Livermore Laboratory Report UCRL-51958, 1976.
4. D. V. ANDERSON, R. H. COHEN, J. R. FERGUSON, B. M. JOHNSTON, C. B. SHARP, AND P. A. WILLMANN, "ORBXYZ: *A 3D Single Particle Orbit Code for Following Charged Particle Trajectories in Equilibrium Magnetic Fields*," Lawrence Livermore National Laboratory Report UCRL-53151, 1981.
5. C. W. GEAR, *Numerical Initial Value Problems in Ordinary Differential Equations*, Prentice–Hall, Englewood Cliffs, N. J., 1971.
6. J. KILLEEN AND K. J. WHITEMAN, *Phys. Fluids* **9** (1966), 1846.
7. D. V. ANDERSON AND J. KILLEEN, *J. Comput. Phys.* **10** (1972), 133.
8. C. L. HEDRICK, G. E. GUEST, AND D. B. NELSON, Oak Ridge National Laboratory Report ORNL-TM-4076, March 1973.
9. L. S. HALL AND B. MCNAMARA, *Phys. Fluids* **18** (1975).
10. R. H. COHEN AND G. ROWLANDS, *Phys. Fluids* **21** (1978), 627.
11. J. H. FOOTE, R. P. FREIS, AND D. FUSS, "*Controlled Thermonuclear Research Annual Report*," Lawrence Livermore Laboratory Report UCRL-50002-67, 1967.
12. J. B. TAYLOR, *Phys. Fluids* **6** (1963), 1529.
13. M. E. RENSINK, *Bull. APS* **21** (1976), 1187.
14. T. A. CUTLER, Lawrence Livermore National Laboratory, private communication, 1979.
15. T. A. CUTLER, L. D. PEARLSTEIN, AND M. E. RENSINK, "*Computation of the Bounce Average Code*," Lawrence Livermore Laboratory Report UCRL-52233, 1977.
16. B. I. COHEN (Ed.), *Status of Mirror Fusion Research 1980*," Lawrence Livermore National Laboratory Report UCAR-10049-80.
17. W. A. PERKINS AND J. C. BROWN, "MAFCO—*A Magnetic Field Code for Handling General Current Elements in Three Dimensions*," Lawrence Livermore Laboratory Report UCRL-7744 Rev. II 1966.

18. J. DOUGLAS AND J. GUNN, *Numer. Math.* **7** (1964), 428.
19. D. W. PEACEMAN AND H. H. RACHFORD, *J. Soc. Ind. Appl. Math.* **3** (1955), 28.
20. R. D. RICHTMEYER AND K. W. MORTON, "*Difference Methods for Initial Value Problems*, Wiley–Interscience, New York, 1967.
21. D. S. KERSHAW, *J. Comput. Phys.* **26** (1978), 43.